

Article

Evaluation of the Airborne CASI/TASI Ts-VI Space Method for Estimating Near-Surface Soil Moisture

Lei Fan ^{1,2}, Qing Xiao ^{1,*}, Jianguang Wen ^{1,3}, Qiang Liu ⁴, Yong Tang ¹, Dongqin You ^{1,2}, Heshun Wang ¹, Zhaoning Gong ⁵ and Xiaowen Li ^{6,†}

¹ State Key Laboratory of Remote Sensing Science, Institute of Remote Sensing and Digital Earth, Chinese Academy of Sciences, Beijing 100101, China; E-Mails: fanlei20088@163.com (L.F.); wenjg@radi.ac.cn (J.W.); tangyong@163.com (Y.T.); youdongqin@mail.bnu.edu.cn (D.Y.); heshun8336@163.com (H.W.)

² University of Chinese Academy of Sciences, Beijing 100049, China

³ Joint Center for Global Change Studies, Beijing 100875, China

⁴ College of Global Change and Earth System Science, Beijing Normal University, Beijing 100875, China; E-Mail: toliuqiang@bnu.edu.cn (Q.L.)

⁵ College of Resource Environment and Tourism, Capital Normal University, Beijing 100048, China; E-Mail: gongzhn@163.com (Z.G.)

⁶ School of Geography, Beijing Normal University, Beijing 100875, China; E-Mail: lix@bnu.edu.cn

† This author has been deceased.

* Author to whom correspondence should be addressed; E-Mail: xiaoqing@radi.ac.cn; Tel.: +86-10-6484-2510; Fax: +86-10-6480-6255.

Academic Editors: Xin Li, Nicolas Baghdadi and Prasad S. Thenkabail

Received: 2 November 2014 / Accepted: 9 March 2015 / Published: 18 March 2015

Abstract: High spatial resolution airborne data with little sub-pixel heterogeneity were used to evaluate the suitability of the temperature/vegetation (Ts/VI) space method developed from satellite observations, and were explored to improve the performance of the Ts/VI space method for estimating soil moisture (SM). An evaluation of the airborne ΔT_s /Fr space (incorporated with air temperature) revealed that normalized difference vegetation index (NDVI) saturation and disturbed pixels were hindering the appropriate construction of the space. The non-disturbed ΔT_s /Fr space, which was modified by adjusting the NDVI saturation and eliminating the disturbed pixels, was clearly correlated with the measured SM. The SM estimations of the non-disturbed ΔT_s /Fr space using the evaporative fraction (EF) and temperature vegetation dryness index (TVDI) were validated by using the SM measured

at a depth of 4 cm, which was determined according to the land surface types. The validation results show that the EF approach provides superior estimates with a lower RMSE ($0.023 \text{ m}^3 \cdot \text{m}^{-3}$) value and a higher correlation coefficient (0.68) than the TVDI. The application of the airborne $\Delta T_s/\text{Fr}$ space shows that the two modifications proposed in this study strengthen the link between the $\Delta T_s/\text{Fr}$ space and SM, which is important for improving the precision of the remote sensing Ts/VI space method for monitoring SM.

Keywords: soil moisture; temperature vegetation dryness index; evaporative fraction; CASI; TASI

1. Introduction

Improving soil moisture (SM) evaluation processes is important for understanding the land-atmosphere exchange process in which the SM content controls evaporation from areas of bare soil and transpiration from vegetated areas [1,2]. Various remote sensing approaches to SM observations have been developed in the last two decades. With the launch of the Soil Moisture and Ocean Salinity (SMOS) satellite [3], a near-surface SM remote sensing method could help study the spatial heterogeneity and temporal dynamics of SM at global or regional scales. The surface reflectance/temperature in the optical domain and the microwave brightness temperature are the main remote sensing measurements used to infer near-surface SM contents and are consistent with *in situ* SM measurements [4–8]. The passive microwave brightness temperature (T_B) is highly sensitive to SM at spatial scales of 25 to 150 km [9]. The spatial scales depend on the antenna size and the altitudes of the low-orbit satellites [10], such as the National Airborne Field Experiment (NAFE) [11], SMOS [3], Aquarius [12] and the future Soil Moisture Active Passive (SMAP) satellites [13]. However, the spatial resolutions of the passive microwave data currently used for retrieving SM are coarse, which are useful in large-scale land surface hydrological processes but lead to insufficient representations of SM spatial-temporal dynamics/variability and uncertainties at small scales. Optical remote sensing satellites offer an improved method for monitoring the spatial characteristics of SM at small scales because they provide 10- to 200-times greater spatial resolutions than microwave satellite platforms. The spatial resolutions of optical satellite instruments for estimating SM can reach 1 km (e.g., MODIS) [14] or 90 m (e.g., ASTER) [15].

Investigations of optical high-spatial-resolution SM show that the four following core algorithms are currently in use: (1) the disaggregation algorithm, which optically provides detailed supplementary data combined with microwave data to produce high-resolution SM maps [16–18]; (2) the empirical relation between vegetation indices(VI)/land surface temperature (T_s) and SM [19]; (3) the apparent thermal inertia (ATI) method [20]; and (4) the SM dryness indices of the T_s/VI space [21]. In these methods, the T_s/VI space is widely used in remote sensing satellites that measure reflectance and thermal radiation to predict SM [22–25] due to its definite physical meaning, convenient calculation without a substantial amount of auxiliary data and its high estimation accuracy for areas of bare soil and vegetation [8,26]. The successful use of the T_s/VI space for estimating SM mainly depends on the correct choice of the dry and wet edges in the T_s/VI space.

However, it is challenging to implement appropriate extraction of the dry and wet edges of the Ts/VI space when two inherent defects of the Ts/VI space are non-negligible. One defect is the saturation of the NDVI, which asymptotically approaches saturation after reaching a certain leaf area index (LAI) [27]. Although NDVI saturation also occurs in optical remote sensing data with coarse spatial resolutions, it is more obvious in higher spatial resolution data (e.g., LANDSAT and ASTER) [8,28–31]. Another defect is the presence of disturbed pixels, which hinders the construction of the Ts/VI space. An ideal Ts/VI space is constructed using three types of pixels: bare soil pixels, vegetation-covered pixels, and mixed pixels with bare soil and vegetation components [21]. Disturbed pixels, such as shadow and building pixels, fail to depict SM status due to their deviations from the ideal Ts/VI space in terms of their incident radiation, albedo and thermal inertia [8]. It is necessary to analyze the defects and uncertainties of the Ts/VI space by using higher spatial resolution remote sensing data with less sub-pixel variability. Such high spatial resolution data can be obtained from aircraft measurements, which are better than satellite data because satellite data average the sub-pixel variability and mask the underlying sub-pixel heterogeneity of SM contents and landscapes [10].

With the implementation of the Heihe Watershed Allied Telemetry Experimental Research project (HiWATER) in 2012 [32], visible/near-infrared reflectance (1 m spatial resolution) and thermal temperature (3 m spatial resolution) measurements based on an airborne platform were collected to understand the applicability of Ts/VI space to the retrieval of SM at higher spatial resolutions and improve the remote sensing performance of the Ts/VI space algorithm. Moreover, aircraft data can cover several satellite footprints each day, allowing the satellite pixels to be simulated to test and improve remote sensing algorithms before applying real satellite platforms [33].

The objectives of this paper are to evaluate the applicability of the Ts/VI space in an SM-estimation method based on the airborne data from the Compact Airborne Spectral Imager (CASI) and the Thermal Airborne Spectrographic Imager (TASI) and to improve the capabilities of the Ts/VI space for monitoring SM. This study is presented as follows. First, the airborne HiWATER experiment and *in situ* measurements are illustrated. Then, we present the Ts/VI space algorithm and propose its reformulation for CASI/TASI SM estimations. Finally, we evaluate the improved airborne Ts/VI space method and the airborne-based SM estimations.

2. Airborne Experiment and SM Measurements

2.1. Study Area and Field Campaign

The study area (Figure 1) was located in an artificial oasis–riparian ecosystem–wetland–desert area in the middle reaches of the Heihe River Basin (HRB) in northwestern China (38.87°N, 100.40°E), where field SM data, meteorological data and airborne remote sensing data were obtained from the HiWATER experiment. The annual precipitation in the artificial oasis is 117 mm, with a high potential evaporation of 1200–1800 mm. Irrigation is the main source of water, and the main crops include maize, wheat and vegetables. HiWATER is an ongoing, watershed-scale, eco-hydrological experiment that is designed from an interdisciplinary perspective to address various problems, such as heterogeneity, scaling, uncertainty and the closed water cycle at the watershed scale [32].

As part of HiWATER, an eco-hydrological wireless sensor network (EHWSN) was installed in a foci experiment area. The EHWSN design is explained in [34,35]. In addition, 48 WATERNET nodes of the EHWSN measured SM, and soil temperature data were obtained for two layers (4 cm and 10 cm). The SM measurements were based on the frequency-domain reflectometry method using Hydro Probe II (HP-II) sensors. In addition, 10 automatic weather stations (AWSs) in the foci experiment area generated observational data, including air temperature (Ta), vapor pressure, wind speed, and SM for seven layers (2 cm, 4 cm, 10 cm, 20 cm, 40 cm, 60 cm, and 100 cm). All nodes selected in this study were located in the cornfield, and the statistics of their fractional vegetation cover based on their airborne footprint (3 m) are listed in Table 1. We chose an area of approximately 4.5 km × 5.0 km that was covered by WATERNET and AWSs as the validation area (Figure 1). Next, 10 AWS SM observations were selected to analyze the relationships between the dryness indices and SM at different SM depths in Section 5.2. In addition, 58 measured SM contents at a depth of 4 cm (10 AWSs and 48 WATERNET nodes) were selected to retrieve and validate the SM. Using a systematic sampling method, 29 nodes were sampled to establish the coefficients of the algorithms presented in Section 3 (the training subsample), and the other 29 nodes were used as validation subsamples in Section 5.3. The distribution of subsamples is displayed in Figure 1.

Table 1. Summary of the WSN data used in the study.

WSN	Node Number	Fractional Vegetation Cover			Underlying Surface
		Range	Mean	Standard Deviation	
AWSs	10	0.21–0.62	0.47	0.09	cornfield
WATERNET	48	0.38–0.68	0.51	0.06	cornfield

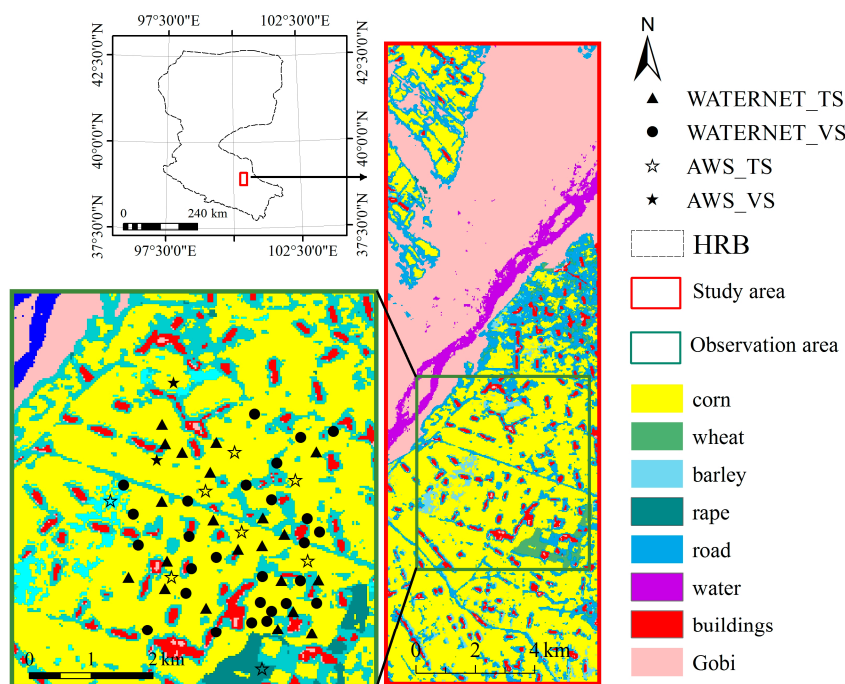


Figure 1. Land classification map of the study area with *in situ* SM measurement points (the WATERNET_TS and AWS_TS nodes are used as the training subsample, and the WATERNET_VS and AWS_VS nodes are used as the validation subsample).

2.2. Airborne Hyperspectral Measurements

The airborne hyperspectral datasets of CASI and TASI were simultaneously acquired on 10 July 2012, between 12:00 and 12:30 (local time) at an altitude of 2500 m to improve the remote sensing methods used for observing key eco-hydrological processes [32]. Table 2 displays the basic specifications of these two sensors.

CASI1500 is a visible and near-infrared pushbroom hyperspectral sensor with 48 bands that cover 380–1050 nm with a ground spatial resolution of 1 m. The raw data were acquired as 14-bit digital values and converted into 16-bit radiances. Geometric corrections were applied using a digital elevation model and ground control points. Atmospheric corrections were applied to produce a reflectivity profile at the pixel level using the ModTRAN model [36]. The processed CASI 1500 data were resampled at a spatial resolution of 3 m to fit the TASI 600 grid.

The TASI 600 sensor is a thermal pushbroom hyperspectral sensor that has a spectral range of 8 to 11.5 μm (32 bands) and a spatial resolution of 3 m. The TASI 600 data were processed using radiometric calibration, geometric correction and atmospheric correction [37]. Atmospheric correction was performed using an atmospheric profile extracted from NCEP data, which was modified by the local meteorological data and ModTRAN5.0 [38]. Land surface temperatures were produced using a modified temperature and emissivity separation (TES) algorithm with an RMSE of less than 1.5 K [39].

Table 2. Basic specifications of CASI/TASI.

Basic Specifications	CASI 1500	TASI 600
Spectral range	380–1050 nm	8–11.5 μm
Spectral resolution	7.2 nm (48 bands)	110 nm (32 bands)
Spectral width	7 nm	15 nm
Scan angle	40°	40°
Across-track pixels	1500	600
Spatial resolution	1 m	3 m

3. Ts/VI Space Algorithm

3.1. Theory of Ts/VI Space

The scatter plot of Ts and VI exhibits a triangular-trapezoidal shape when the study area contains a wide range of fractional vegetation cover and SM. The conceptual Ts/VI space is shown in Figure 2, where VI is plotted on the x -axis and Ts is plotted on the y -axis. The dry edge (AB) represents minimum SM or evapotranspiration, with low SM in the root zone under the full range of fractional vegetation cover conditions. Along the dry edge, the maximum values of Ts decrease as the fractional vegetation cover increases. The horizontal wet edge (BC) represents the maximum soil wetness conditions and potential evapotranspiration. The left edge represents bare soil, which ranges from dry to wet and from maximum to minimum Ts. The Ts/VI space method has been widely used to estimate evapotranspiration and SM [7,21,40,41].

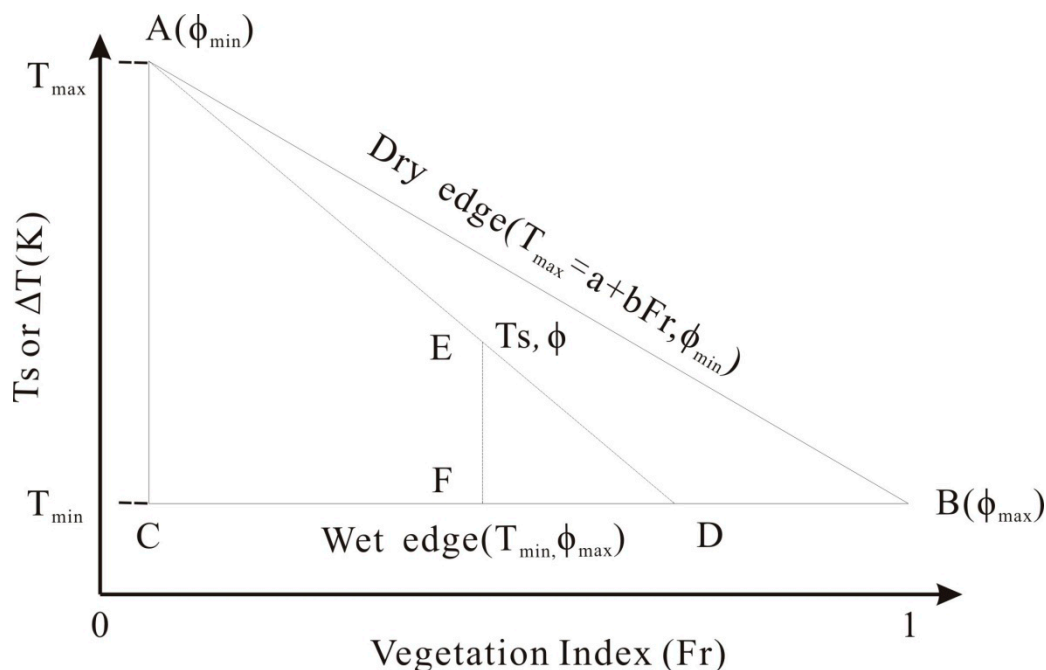


Figure 2. A theoretical diagram of the surface temperature/vegetation index space.

Soil moisture and evapotranspiration mechanisms mainly determine the locations of pixels in the Ts/VI space [8,21]. The fractional vegetation cover can be represented by VI, which determines the proportion of bare soil and vegetation visible to a sensor. Differences in radiative temperatures between the soil and canopy affect the spatially integrated Ts, which is largely controlled by evapotranspiration (ET, also denoted as LE) and is used to determine the surface energy balance as follows:

$$R_n = LE + H + G \quad (1)$$

where R_n , LE, H, G are the net radiation, evapotranspiration, sensible heat flux and soil heat flux, respectively, and the units of all fluxes are $W \cdot m^{-2}$. In addition, the LE and H are partly influenced by the stomatal resistance to transpiration, which is partly controlled by the availability of SM [42]. Furthermore, Ts is partly affected by thermal inertia, which controls the heat flow into G, and the thermal inertias related to the SM content. The available energy incident at the surface ($R_n - G$) affects Ts [15]. The radiative control of Ts indicates that the surface exhibits a higher temperature with a higher net shortwave radiation balance, such as a low albedo, which is a function of the SM content, soil type and fractional vegetation cover. In addition, the $R_n - G$ is a driving force for ET. Thus, the interactions between ET and Ts are controlled by R_n , H, and G, which are all influenced by SM availability. Thus, ET is allowed to predict SM availability in the Ts/VI space.

Based on the Ts/VI space, a number of evapotranspiration indices and soil dryness indices have been proposed for assessing ET and SM [7,8,43]. The evaporative fraction (EF) was introduced as an evapotranspiration index for parameterizing ET. In addition, the EF was generally more stable during the day than ET and was regarded as a more suitable indicator of SM relative to ET [44]. Furthermore, the EF can be calculated using ancillary data combined with the Ts/VI space. Soil dryness indices were also proposed by simplifying the ET models. The most widely applied soil dryness index, the temperature vegetation dryness index (TVDI), was proposed by simplifying the evapotranspiration rate [14,24,25,44]. The TVDI can be obtained by using the Ts/VI space.

One inherent assumption of the Ts/VI space is that the air temperature (T_a) is considered constant for the selected study area, which results in errors for larger areas. The T_a incorporated in the Ts/VI space was used to correct the error by replacing Ts with the Ts- T_a term (ΔT_s) [23,45]. The ΔT_s value is calculated as the difference between the surface temperature and the air temperature, and represents the energy exchange at the earth's surface. In addition, VI (such as NDVI) is a greenness variable that characterizes the degree of vegetation cover and can be replaced by the fractional vegetation cover (Fr), which presents the relative abundance of vegetation within a pixel [46]. Furthermore, Fr is calculated from NDVI by using the following equation [47]:

$$Fr = (NDVI - NDVI_{min}) / (NDVI_{max} - NDVI_{min}) \quad (2)$$

where $NDVI_{max}$ is the NDVI of full vegetation ($Fr = 1$), which can be calculated from the maximum NDVI in the study area, and $NDVI_{min}$ is the NDVI of the bare soil ($Fr = 0$), which can be obtained from the minimum NDVI in the study area, excluding the NDVI in the water bodies [31]. Therefore, Fr and ΔT_s were used to construct the ΔT_s /Fr space in this research.

3.2. SM Estimation from EF

EF is defined as the ratio of ET to the available energy (Rn-G), where ET and Rn-G imply a strong relationship with the SM contents mentioned above. An algorithm proposed by Jiang [48] is used to estimate the EF and ET values because it obtains satisfactory accuracy with a few input variables, where EF is estimated as a function of the Priestley-Taylor parameter as follows [48]:

$$EF = \phi \frac{\Delta}{\Delta + \gamma} \quad (3)$$

where ϕ is the so-called Priestley-Taylor parameter, Δ is the slope of the saturated vapor pressure and T_a ($\text{hPa} \cdot \text{K}^{-1}$), and γ is the psychrometric constant ($\text{hPa} \cdot \text{K}^{-1}$). Furthermore, Δ and γ were calculated using the relationships given by [49] and the T_a , vapor pressure and wind speed.

In Jiang's model [48], the Priestley-Taylor parameter ϕ is estimated by using a two-step linear interpolation scheme and the Ts/VI space, as shown in Figure 2 [23]. The dry edge is defined by the maximum ΔT_s (T_{max}), and the wet edge is defined by the minimum ΔT_s (T_{min}). In addition, the ϕ value varies from $\phi_{min} = 0$ (along the dry edge line) to $\phi_{max} = 1.26$ (along the wet edge line). Point A represents $Fr = 0$ and T_{max} , and point B represents $Fr = 1$ and T_{min} . For ϕ at point E, the length of AE represents $\phi_{min} - \phi$, while the length of AD is $\phi_{max} - \phi_{min}$. Thus, considering the similarity between EFD and ADC, the ϕ value for any point in the Ts/VI space can be estimated as follows:

$$\phi = \frac{T_{max} - \Delta T_s}{T_{max} - T_{min}} (\phi_{max} - \phi_{min}) + \phi_{min} \quad (4)$$

where ΔT_s represents Ts- T_a , and T_a is the observed air temperature from the AWSs. As shown in Figure 2, the wet edge (BC) for a given Fr is calculated by averaging a group of points in the lower limits of the ΔT_s /Fr space. The dry edge is modeled using a linear empirical fit to Fr. The ϕ_{max} value is constant and equal to 1.26 at the wet edge, and ϕ_{min} is denoted as follows:

$$\phi_{min} = 1.26Fr \quad (5)$$

Next, EF is converted to SM using the Lee model, which has taken into account the water transport from the inner soil pores to the soil surface and the soil hydraulic conductivity [45,50]. The Lee model can be expressed as follows:

$$SM = \begin{cases} \frac{\theta_{fc}}{\pi} \cos^{-1}(1 - 2EF^{0.5}), & EF < 1 \\ \theta_{fc}, & EF \geq 1 \end{cases} \quad (6)$$

where SM is the remotely sensed volumetric SM content that represents a soil layer of several centimeters in depth [50,51] and θ_{fc} is the volumetric SM content at field capacity. The soil in the study area has a silt loam texture, and a θ_{fc} of $0.35 \text{ m}^3 \cdot \text{m}^{-3}$.

In the EF estimation model, the dry and wet edges are assumed to represent the minimum and maximum ET values, respectively. The T_s varies from a minimum (T_{\min} , Φ_{\max}), with the strongest evaporative cooling, to a maximum (T_{\max} , Φ_{\min}), with the weakest evaporative cooling. Therefore, the dry edge represents the minimum EF, and the wet edge represents the maximum EF. The model is valid when the minimum and maximum ET values can both be observed within the boundaries of the study area. One important assumption is that these variations largely result from differences in SM availability. Assuming that the soils in the study area should have some of the same fixed soil-water characteristics [50], the Lee model for estimating SM was proposed by studying the quantitative relations between the field EF and *in situ* SM measurements.

3.3. SM Estimations from the TVDI

The TVDI was proposed by simplifying the evapotranspiration rate, which is important for the ET estimation model. The TVDI depends on an empirical parameterization of the T_s/VI space that is completely based on remote sensing data. As shown in Figure 3, it was assumed that the dry edge represents the driest surface soil conditions when $TVDI = 0$, and the wet edge represents the wettest soil conditions when $TVDI = 1$. If the SM varies linearly from the dry edge to the wet edge of the T_s/VI space, the TVDI is formulated as follows:

$$TVDI = (\Delta T_s - T_{\min}) / (T_{\max} - T_{\min}) \quad (7)$$

where the definitions of ΔT_s , T_{\min} , and T_{\max} are the same as those described for Equation (4). The isolines of the TVDI in Figure 3 represent the equal availability of surface moisture and take on values between the maximum SM (SM_{\max}) and minimum SM (SM_{\min}) contents. By obtaining SM_{\max} at the surface along the wet edge and SM_{\min} along the dry edge, the TVDI can be converted to near-surface SM by using the following formula [15,52]:

$$SM = SM_{\min} + TVDI \times (SM_{\max} - SM_{\min}) \quad (8)$$

where SM_{\max} can be set as equal to the field capacity in most cases, and SM_{\min} is equal to the permanent wilting point [53]. In this study, the coefficients of least square regression between the *in situ* SM and the remotely sensed TVDIs were used to derive SM_{\max} and SM_{\min} throughout the study region.

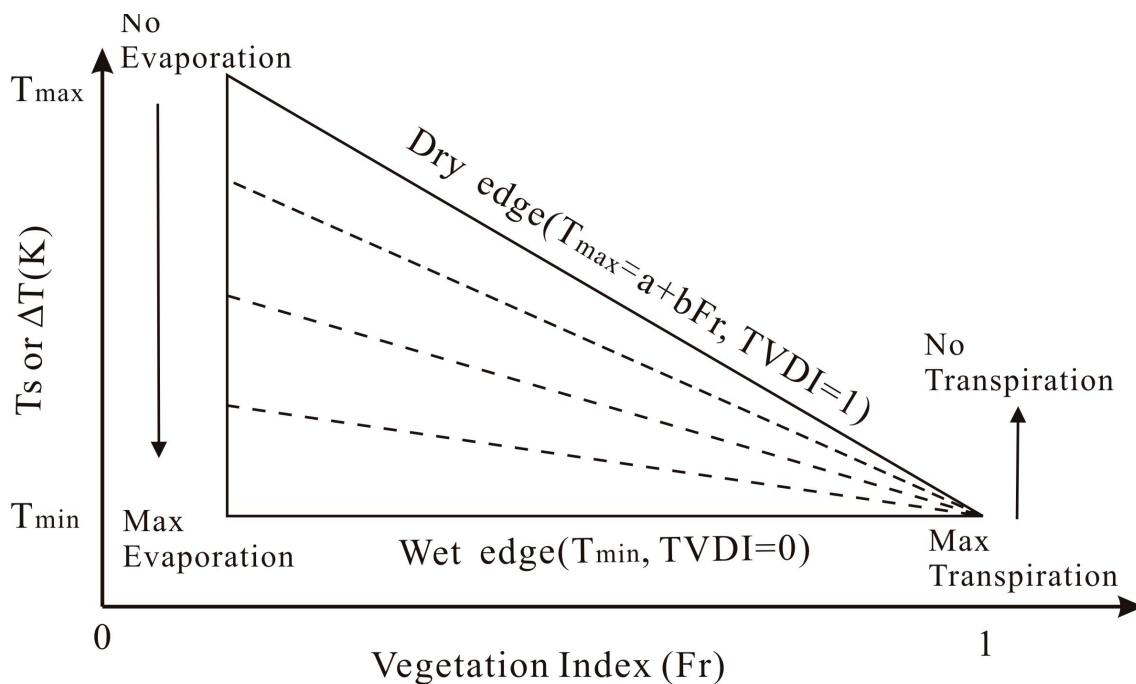


Figure 3. Conceptual diagram of the Ts–VI triangle for determining the TVDI.

In this study, the applicability of airborne $\Delta T_s/Fr$ space to assessing the surface SM was evaluated and proposed to improve the precision of the Ts/Fr space for monitoring SM. Figure 4 shows a flowchart in which the $\Delta T_s/Fr$ space incorporating T_a was built using CASI, TASI and AWS data. Next, the $\Delta T_s/Fr$ space was adapted using NDVI de-saturation and by eliminating disturbed pixels with land use and land cover change data (LUCC). At the airborne level, a reasonable construction of the Ts/Fr space could be interfered with by the disturbed pixels and the saturation of Fr caused by the saturation of the NDVI at high LAIs. These characteristics could affect the EF and TVDI when estimating the SM content. We attempted to use the airborne Ts/VI space to accurately estimate the EF and TVDI and further improve their performances in the SM estimation process. Then, based on the improved $\Delta T_s/Fr$ space, the TVDI and EF were calculated to obtain the airborne SM. Finally, the resulting SM estimates were validated using WSN to determine the effectiveness of using the improved airborne Ts/VI space for monitoring SM.

4. The Adaption of Airborne Ts/VI Space

4.1. De-saturated $\Delta T_s/Fr$ Space ($\Delta T_s/Fr_D$ Space)

As shown in Figure 5, the raw $\Delta T_s/Fr$ space (green scatter plot) from the CASI and TASI data forms an irregular trapezoid, indicating that the non-linear downward trend at Fr is greater than 0.8. Considering the calculation of Fr from Equation (1) based on the NDVI, the non-linear trend may result from NDVI saturation. This trend could result in extraction errors at the dry edge at high Fr values and affect the accuracy of the SM estimation. Thus, the de-saturated $\Delta T_s/Fr$ space ($\Delta T_s/Fr_D$) was proposed for describing the actual Fr conditions for the areas with high vegetation coverage.

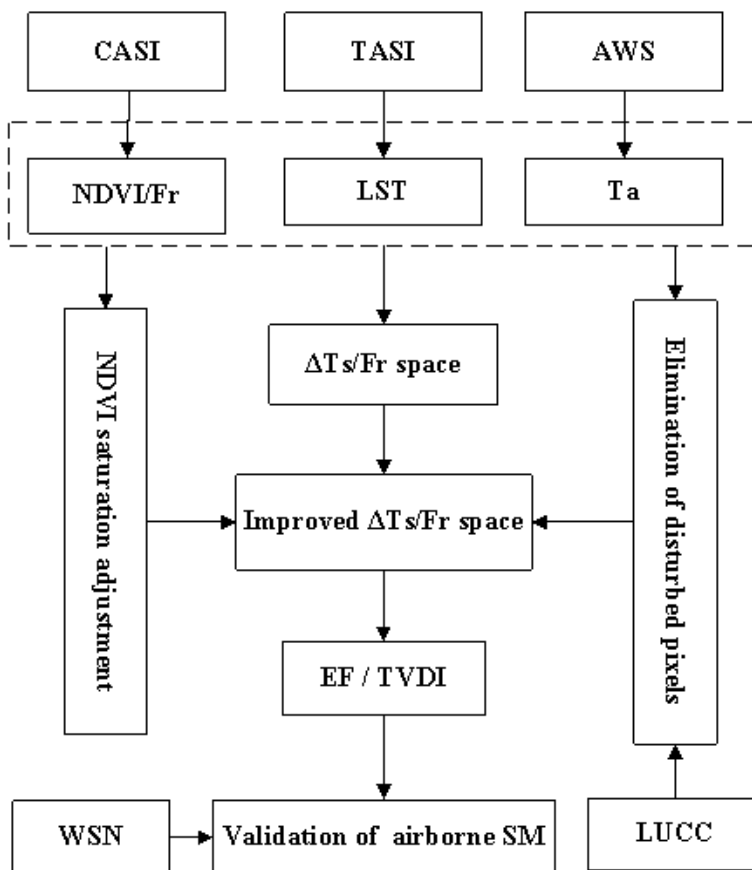


Figure 4. Algorithm flowchart for this research.

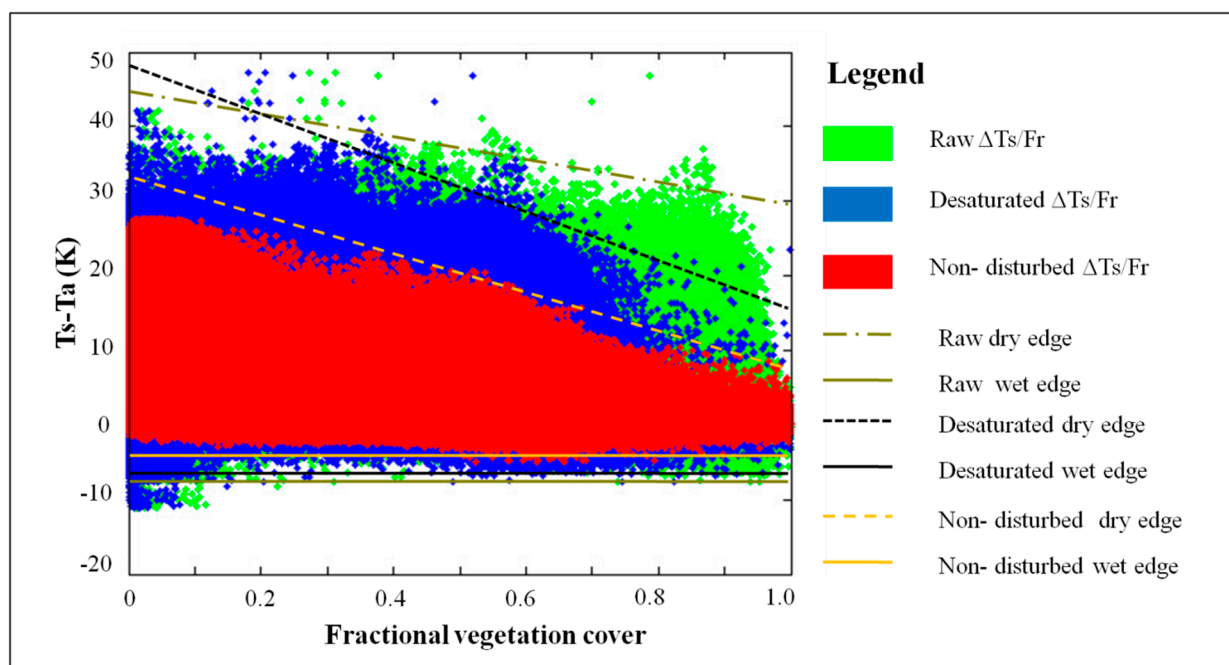


Figure 5. The initial and improved $\Delta T_s/F_r$ space.

In the de-saturated $\Delta T_s/F_r$ space, the NDVI saturation effect is reduced based on the different sensitivities of the ratio vegetation index (RVI) and NDVI to the LAI [15]. The NDVI is more sensitive to moderate and low LAIs (where $NDVI < 0.78$), and the RVI is more sensitive to high LAIs

(where the NDVI > 0.78). In addition, the NDVI and RVI exhibit similar sensitivities to LAI when the NDVI is between 0.75 and 0.85. As shown by the regression analysis of the relationship between the RVI and NDVI when the NDVI is between 0.75 and 0.85 (Figure 6), Equation (9) was used to predict the de-saturated NDVI when the raw NDVI was greater than 0.78 (where the NDVI is less sensitive to the corn field LAI [30]). The de-saturated $\Delta T_s/F_r$ space is shown in Figure 5 (blue scatter plot).

$$\text{NDVI}_D = \text{RVI} \times 0.016 + 0.65 \quad (9)$$

where NDVI_D is the desaturated NDVI. The RVI can be calculated using the ratio between the near-infrared reflectance and the visible red reflectance.

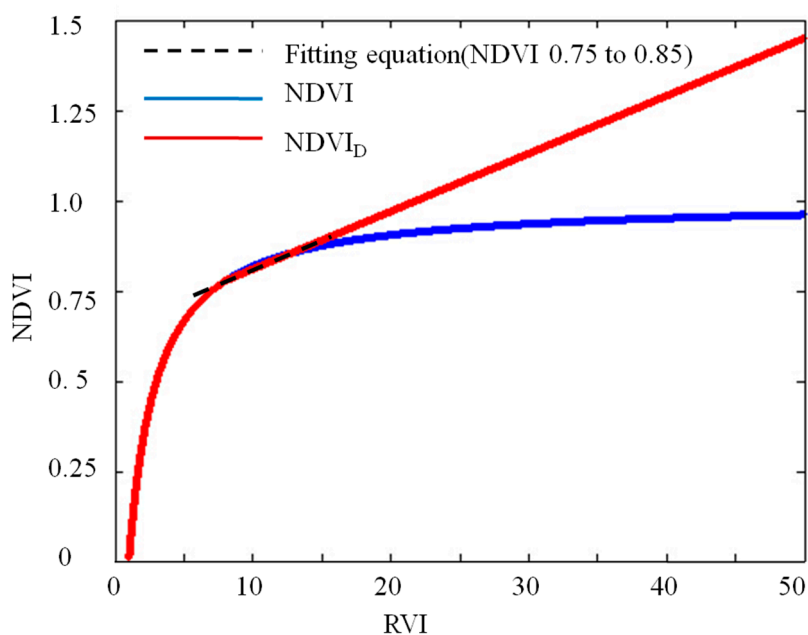


Figure 6. The result of the desaturated NDVI by the RVI.

4.2. Non-Disturbed $\Delta T_s/F_r$ Space ($\Delta T_s/F_{rN}$ Space)

An ideal $\Delta T_s/F_r$ space is composed of pixels from three main land types: bare soil, full-cover vegetation, and a mixture of bare soil and vegetation. Coarse satellite data can include some mixed pixels, in which other types of land only contributes lightly to the final radiation of the pixels. However, in the airborne data with a 3-m spatial resolution, many pixels are dominated by other land cover types, which make it difficult to estimate the SM content. These pixels, such as houses, roads, shaded roads and shaded trees, are defined as “disturbed pixels” (Figure 7). Artificial facilities, such as greenhouses, buildings and roads (pathways) may also result in the overestimation of the dry edge because the land surface temperature is higher than that of the bare soil. Shadowed pixels have lower incident radiation than sunlit pixels for the same surface types, which affects the F_r and T_s . Thus, the F_r and T_s of shadowed pixels are lower than those of sunlit pixels, resulting in the underestimation of dry and wet edges. A complete tree crown is composed of a sunlit side and a shaded side in the airborne data, which indicates that a single pixel in the $\Delta T_s/F_r$ space cannot reflect the SM content in the root zone of a tree. Although the F_r saturation is solved in the $\Delta T_s/F_{rD}$ space, these disturbed pixels will affect the construction of the $\Delta T_s/F_r$ space, resulting in uncertainty and errors in the

observed dry and wet edges. Therefore, disturbed pixels should be eliminated to improve the SM estimations from remotely sensing data. The approach used for removing the disturbed pixels is described as follows:

- (1) Artificial facility pixels. The building and road pixels were recognized by LUCC data based on the same CASI data provided by HiWATER [54]. Many pathway pixels between farmlands were too shallow to display in LUCC data and were removed in step (4).
- (2) Shadowed pixels. The shadowed pixels were identified when their pixel reflectance values in the 554-nm CASI band were less than 0.027 [54].
- (3) Tree pixels. Woods were extracted when the areas were $>20 \text{ m}^2$ and when the reflectance variance in the CASI 554-nm band was >0.025 . Green belts were identified when the ratio of the girth to the area was >0.38 and when the height was $>15 \text{ m}$ by using the vegetation height product with a spatial resolution of 1-m from the digital surface model [55].
- (4) Pathway, greenhouse, and outlier pixels. The common characteristics of these pixels were that they were all distributed in farmland. The pixels' T_s were much greater than the neighboring farmland pixels, and their NDVI values were much lower. Based on these characteristics, belt transect pixels covering areas of $1 \text{ km} \times 1 \text{ km}$ were used to calculate the variance of T_s (D_{T_s}), and the NDVI variance (D_{NDVI}) of each pixel. Combined with ground surveys and visual interpretations, the pixels with D_{NDVI} values less than 0.15 or D_{T_s} values greater than 20 K^2 were defined as disturbed pixels. Then, the pathway, greenhouse, and outlier pixels were removed from the study region using a $1 \text{ km} \times 1 \text{ km}$ window size and thresholds of D_{NDVI} and D_{LST} .

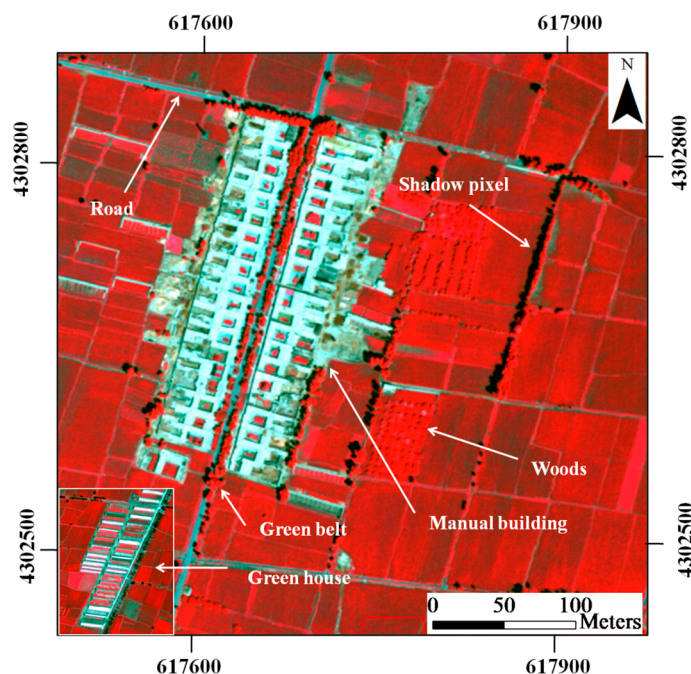


Figure 7. The distribution of disturbed pixels from the CASI data (red band: 855 nm, green band: 645 nm, and blue band: 552 nm).

The red scatter plot in Figure 5 shows the non-disturbed $\Delta T_s / Fr$ space ($\Delta T_s / Fr_N$) after removing the disturbed pixels. The non-disturbed dry edge was lower than the raw dry edge, and the

non-disturbed wet edge was greater than the raw wet edge. The non-disturbed lower dry edge could be attributed to the removal of artificial facility pixels. Under conditions of similar fractional vegetation cover, the noon-Ts values of the cement buildings, greenhouses and asphalt/concrete roads were higher than those of the bare soil due to evaporative control [15]. This result occurred because the bare soil is cooled by SM through evaporation [15], while the buildings, greenhouses and asphalt/concrete roads are impervious surfaces from which evaporative cooling is scarce [56,57]. Furthermore, the building and road pixels, which are mixed with forest and grassland components, have higher noon-Ts than the mixed pixels that include bare soil and vegetation at the same Fr [56].

5. Results

5.1. Analysis of $\Delta T_s/Fr$ Space

Figure 5 shows the raw, de-saturated and non-disturbed $\Delta T_s/Fr$ space. The raw $\Delta T_s/Fr$ space (green scatter plot) exhibits an irregular trapezoid shape and Fr saturation when $Fr > 0.8$, and the corresponding dry and wet edges exhibit the worst fits with the lowest $r^2 < 0.38$ (Table 3). Thus, the raw $\Delta T_s/Fr$ space fails to describe the SM content when $Fr > 0.8$. The de-saturated $\Delta T_s/Fr$ space (blue scatter plot) shows the Fr saturation effect of the dense vegetation canopies being removed. The dry and wet edges are a better fit compared with the raw $\Delta T_s/Fr$ space (with a higher r^2 , as shown in Table 3). After eliminating the disturbed pixels based on the de-saturated $\Delta T_s/Fr$ space, the non-disturbed $\Delta T_s/Fr$ space (red scatter plot) results in the best extraction of the dry and wet edges and the highest r^2 , particularly in terms of the non-disturbed dry edge ($r^2 = 0.96$, Table 3). We conclude that after the NDVI desaturation and the elimination of the disturbed pixels, the non-disturbed $\Delta T_s/Fr$ space can be constructed reasonably, which contributes to the accuracy of the TVDI and EF estimations.

In addition, a narrower divergence in the non-disturbed $\Delta T_s/Fr$ space was observed relative to the other two spaces (Figure 5). The lower dry edge may result from the elimination of disturbed pixels with high Ts, such as roads, greenhouses, and green belts. The rising wet edges may result from the removal of disturbed pixels with low Ts, such as shadows.

Table 3. The statistics of the dry and wet edges.

$\Delta T_s/Fr$	Dry/Wet Edge	Fitting Equation	r^2
Raw $\Delta T_s/Fr$	Dry edge	$y = -14.7x + 44$	0.38
	Wet edge	$y = 1.587x - 7$	0.25
$\Delta T_s/Fr_D$ space	Dry edge	$y = -30x + 47.1$	0.78
	Wet edge	$y = 0.72x - 7.5$	0.31
$\Delta T_s/Fr_N$ space	Dry edge	$y = -23.05x + 32$	0.96
	Wet edge	$y = -0.16x - 3$	0.57

5.2. The Relationships between Dryness Indices and SM Contents at Different Depths

One important prerequisite for the SM estimation process is the choice of the measured SM depth for validating the dryness index estimates. In this study, the validated SM depth was determined by conducting a correlation analysis between the dryness indices from the three $\Delta T_s/Fr$ spaces and the *in situ* measurements of SM from 10 AWSs at different depths.

The correlation analysis results are displayed in Table 4, and the correlations were evaluated using the linear model for the TVDI and the Lee model for the EF. Table 4 shows that the TVDI and EF exhibit relationships with the measured SM at a depth of 4 cm and a weak relationship at a depth of 2 cm. These findings may result from AWSs located at the mixed land surfaces of the bare soil and vegetation due to the Fr of the AWS pixels between 0.21 and 0.62 (Table 1). At the mixed land surface, the dryness indices reflect the soil water contents that were determined by the vegetated root zone (0–20 cm) and the top (0–5 cm) or thin layer (~1 mm) of the bare soil [58]. Therefore, *in situ* measurements at a depth of 4 cm were selected from 10 AWSs and 48 WATERNET nodes to retrieve and validate the SM content in Section 5.3 by considering the AWSs and WATERNET nodes with similar surface conditions (Table 1). The details of the sampling strategy were introduced in Section 2.1 and are displayed in Figure 1. A similar SM depth was used by other researchers to validate the EF and TVDI estimates [10,15,23].

Table 4. The correlation analysis of the dryness indices with different SM depths.

SM Depth	EF _N	TVDI _N	EF _D	TVDI _D	EF _{raw}	TVDI _{raw}
	r^2	r^2	r^2	r^2	r^2	r^2
SM at a depth of 2 cm	0.38	0.39	0.3	0.32	0.2	0.21
SM at a depth of 4 cm	0.6	0.53	0.45	0.43	0.11	0.24
SM at a depth of 10 cm	0.14	0.19	0.15	0.14	null	0.17
SM at a depth of 20 cm	0.13	0.12	null	0.12	null	null
SM at a depth of 40 cm	null	null	null	null	null	null
SM at a depth of 60 cm	null	null	null	null	null	null
SM at a depth of 100 cm	null	null	null	null	null	null

Notes: Values less than 0.1 were defined as null. r^2 is the coefficient of determination. TVDI_{raw} and EF_{raw} were obtained from the raw $\Delta T_s/F_r$ space, TVDI_D and EF_D were obtained from the $\Delta T_s/F_{rD}$ space, and TVDI_N and EF_N were obtained from the $\Delta T_s/F_{rN}$ space.

In addition, no relationship between the dryness indices and the field SM contents at depths of more than 20 cm can be attributed to the fact that SM contents at depths of 0–20 cm were the main water source during the maize maturation stage when 80% of the maize roots were distributed within the upper 0–20 cm of the soil [59].

The results of the correlations at a depth of 4 cm are presented in Figure 8. No significant relationship was found between the *in situ* measurements and the dryness indices from the raw $\Delta T_s/F_r$ space. However, the de-saturated EF and TVDI values were obviously related to the *in situ* measurements (the r^2 values of the TVDI and EF were 0.43 and 0.45, respectively). Thus, adjusting the NDVI saturation enhances the sensitivity of the $\Delta T_s/F_r$ space to the SM content, particularly in vegetation-covered areas. Furthermore, the TVDI and EF values from the non-disturbed $\Delta T_s/F_r$ space exhibit higher correlations with the *in situ* measurements, with r^2 values of 0.53 and 0.6 for the TVDI and EF, respectively. This finding demonstrates that eliminating the disturbed pixels further improves the correlation by removing their influences on the observed dry and wet edges. In conclusion, adjusting the NDVI saturation and eliminating the disturbed pixels can improve EF and TVDI performance when estimating SM. Therefore, the non-disturbed TVDI and EF can be used as better

proxies for SM relative to raw and de-saturated dryness indices. The SM estimates from the non-disturbed dryness indices are shown in the next section.

In addition, as shown in Figure 8, the linear relationship between SM and the TVDI was negative, and the relationship between SM and EF was explained by a cosine function. These results correspond with the observations presented in other studies [45,50]. Therefore, the negative linear model was used for the TVDI and the cosine model (Lee model) was used for the EF to obtain the SM contents.

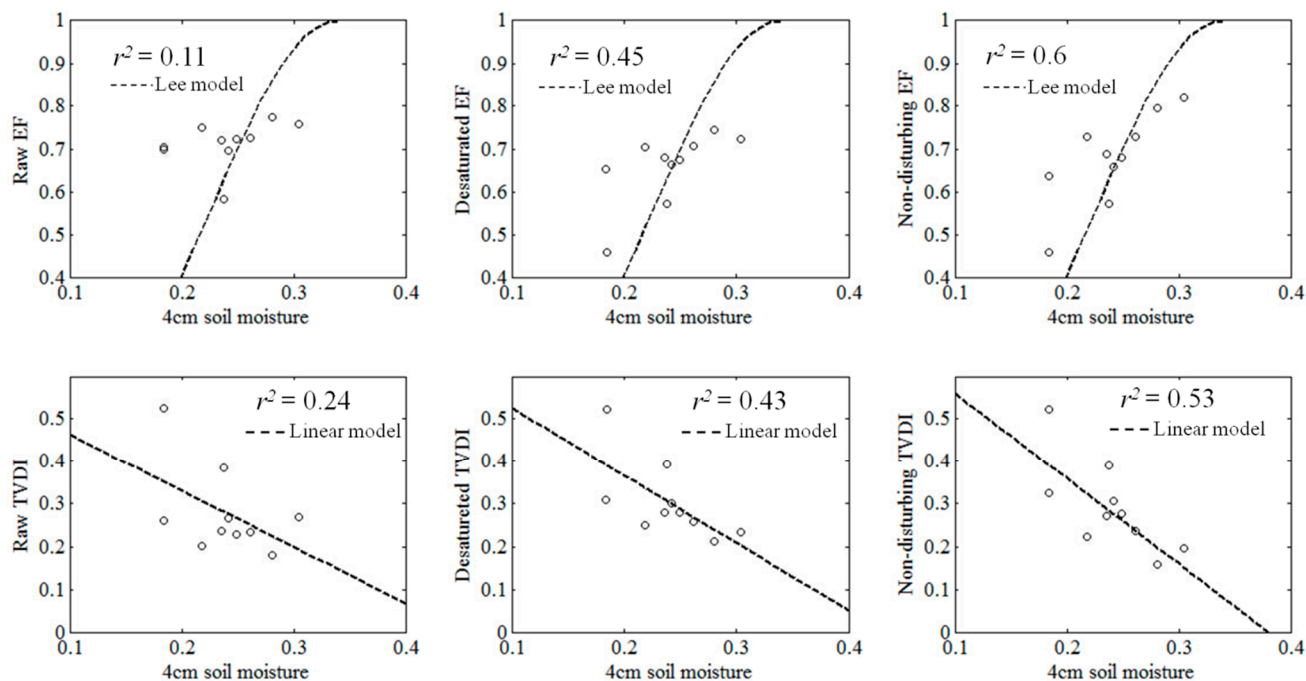


Figure 8. Correlation between the dryness indices and the SM measured at a depth of 4 cm.

5.3. Validation and Evaluation of the Estimated SM

The SM was estimated at a spatial resolution of 3 m using the TVDI and EF generated from the non-disturbed $\Delta T_s/F_r$ space from the CASI and TASI data. The results are displayed in Figure 9, and the corresponding statistics are shown in Table 5. Overall, the results show that the spatial distribution of the TVDI estimates is similar to that of the EF estimates. For example, the Gobi is located at an area with low SM, and the crops are located in areas with high SM. In addition, the crops exhibit different SM patterns due to differing irrigation patterns. The estimates in the validation area show the similarly spatial distribution pattern in Figure 10. However, as observed in Table 5, a greater dynamic range of the EF estimates ($0.002\text{--}0.35\text{ m}^3\cdot\text{m}^{-3}$) with a larger standard deviation ($0.092\text{ m}^3\cdot\text{m}^{-3}$) is found relative to the range ($0.01\text{--}0.336\text{ m}^3\cdot\text{m}^{-3}$) and standard deviation ($0.075\text{ m}^3\cdot\text{m}^{-3}$) of the TVDI estimates. Similarly, the EF estimates in the validation area exhibit a wider range and higher standard deviation for SM when compared with the TVDI estimates. In addition, some null pixel outputs can be observed in Figures 9 and 10 due to the removal of disturbed pixels and noise pixels in Section 3.3.

For validation, Figure 11 shows a comparison of the non-disturbed EF and TVDI estimates with the SM contents measured *in situ*. In addition, the error statistics (bias, mean absolute error (MAE), root mean square error (RMSE) and correlation coefficient (r)) are summarized in Figure 11. Compared with the TVDI, smaller errors were obtained for the SM estimates from the EF regarding the MAE

($0.019 \text{ m}^3 \cdot \text{m}^{-3}$), RMSE ($0.023 \text{ m}^3 \cdot \text{m}^{-3}$) and a high correlation coefficient (r) of 0.67. These validation results suggest that the EF performs better for estimating SM in the study area and that the EF estimates provide sufficient accuracy that is comparable to other international studies using airborne and satellite data [53].

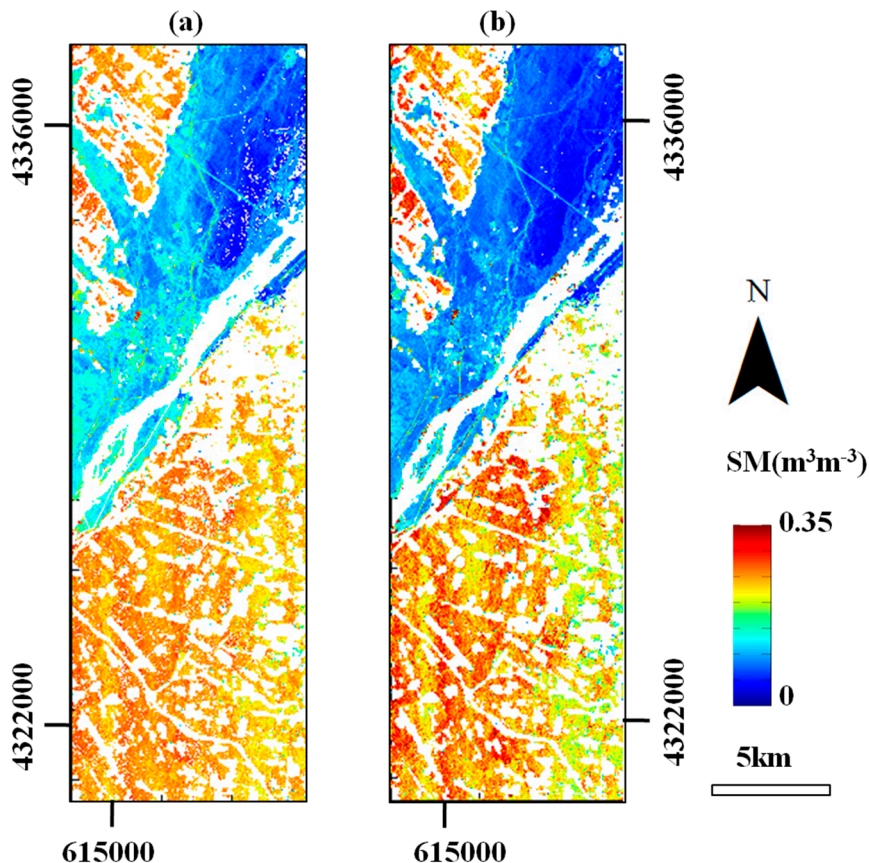


Figure 9. SM estimations in the study area. (a) The SM estimation from EF_D based on $\Delta T_s / Fr_D$ space. (b) The SM estimation from $TVDI_D$ based on the $\Delta T_s / Fr_D$ space.

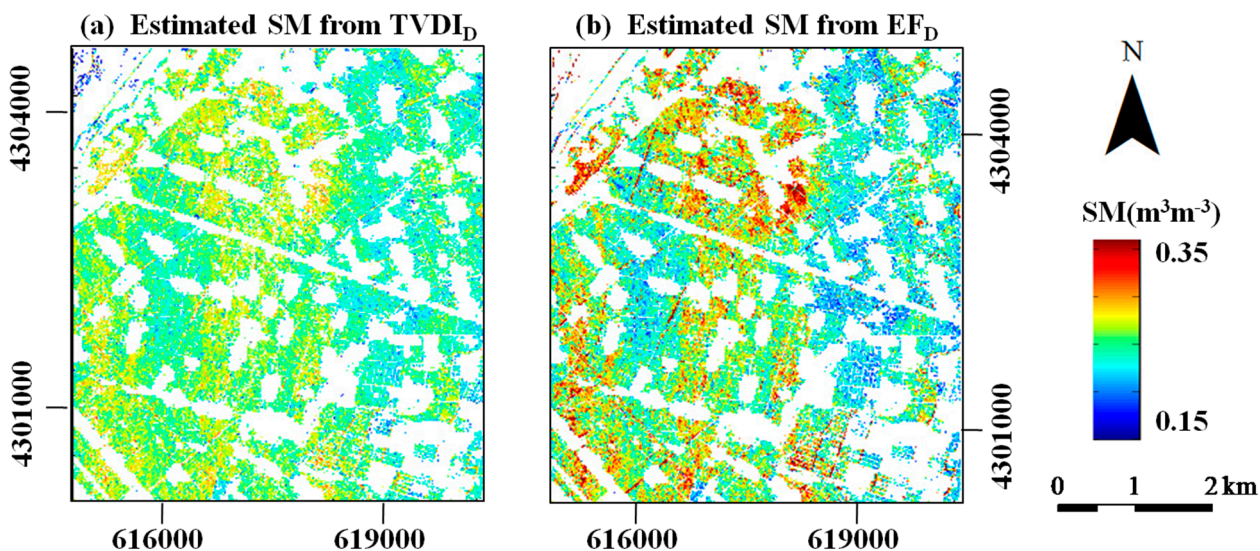
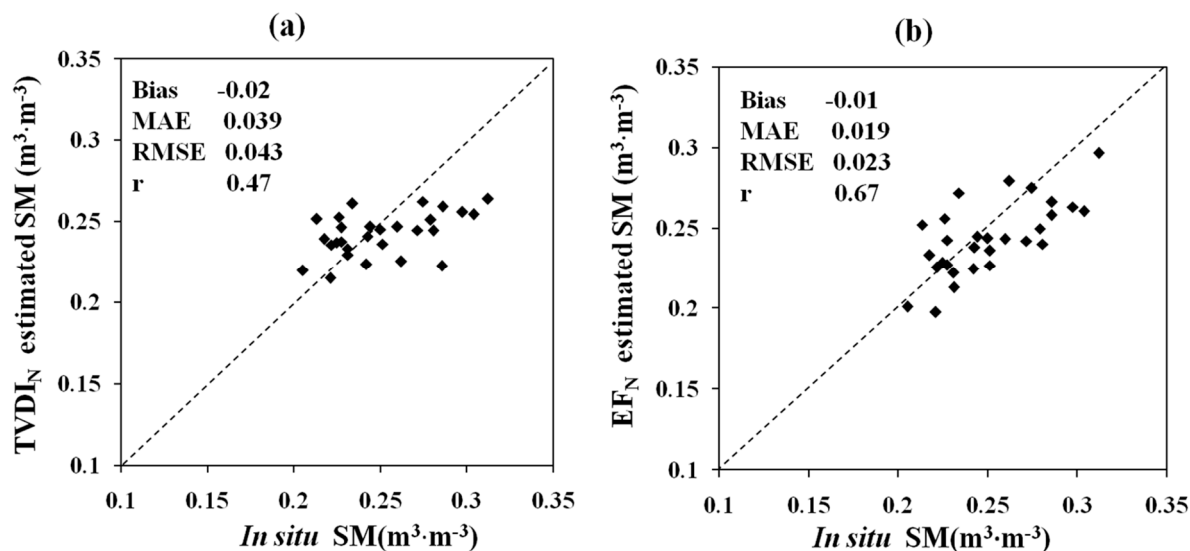


Figure 10. SM estimation in the validation area.

Table 5. Statistical analysis of the SM content from TVDI_N and EF_N.

Soil Moisture (m ³ ·m ⁻³)	Study Area			Validation Area		
	Range	Mean	Standard Deviation	Range	Mean	Standard Deviation
TVDI _N	0.01–0.336	0.188	0.075	0.15–0.336	0.251	0.021
EF _N	0.002–0.35	0.171	0.092	0.15–0.35	0.260	0.040

**Figure 11.** Validation of SM estimates from (a) TVDI_N and (b) EF_N.

6. Discussion

The proposed adaption of airborne $\Delta T_s/F_r$ space in this study is valuable for improving the remote sensing Ts/VI space algorithm for precise SM products. This work proposed that NDVI saturation resulted in the inappropriate extraction of dry edges, which exist in low-to-medium spatial resolution satellite data (e.g., AVHRR and MODIS) from dense vegetation canopies and more evidently in satellite data with a high spatial resolution (e.g., ASTER and LANDSAT). Therefore, the remotely sensed NDVI data are likely desaturated for the appearance of NDVI saturation before constructing the Ts/VI space. However, our implicit assumption is that the saturated ranges of NDVI for different vegetation types are the same. Possible future research would be to further ascertain the range for each vegetation type and select the referenced de-saturated method.

The accurate SM estimate from the non-disturbed $\Delta T_s/F_r$ space implies that the disturbed pixels should be identified and removed using similar or higher spatial resolution LUCC data to build a reasonable Ts/VI space. Similar spatial resolution LUCC data can be used to identify and remove disturbed pixels. If LUCC data are available with a higher resolution and for more land use types and detailed land use classifications, it could be more beneficial to remove some mixed pixels containing buildings or other disturbed types of land.

Incorporating Ta into the $\Delta T_s/F_r$ space could enhance the sensitivity of dryness indices for SM. The Ts/Fr space (without considering Ta) assumes that Ta is constant for the window selected for constructing the space. However, this assumption ignores the heterogeneity of Ta and increases the errors in the TVDI and EF estimations [5]. However, incorporating Ta into the $\Delta T_s/F_r$ triangle space addresses this inconsistency by retrieving the evaporation and transpiration statuses. The Ts-Ta

gradient on the y-axis of the $\Delta T_s/Fr$ space is physically more accurate because it forces the scatter plot of the data to resemble that described in [7,23].

It was also indicated that EF outperformed TVDI in terms of estimating the SM. Note that the excellent performance of the EF depends on the accuracy of the remotely sensed EF estimation from the $\Delta T_s/Fr$ space and on the appropriate model used to obtain the SM. The remotely sensed EF values rely on the accurate extraction of wet and dry edges, because the accurate extraction is beneficial for estimating extreme SM values over a wide range of Fr. The dry and wet edges were accurately extracted in this study after adjusting the NDVI saturation and eliminating the disturbed pixels. Furthermore, quantitative relationships between ground-measured EF and SM values have been studied and properly described using various models. For example, Lee's model was developed for SM estimations at soil depths of more than 2 cm and produced satisfactory estimates [50]. Although the θ_{fc} value impacts the SM estimation of EF in Lee's model, this estimation can be improved by collecting a number of field SM measurements during extremely dry and wet conditions. Therefore, the EF has better potential as an index than the TVDI for monitoring dry conditions and SM at regional or global scales when supported by weather stations data. However, the remotely sensed EF algorithm is based on the assumption that differences in surface temperature primarily result from evaporation for a given net radiation and atmospheric condition [50]. To apply the algorithm over large areas, it is preferential to use normalized forms of T_s and VI to minimize the effects of heterogeneous net radiation and the complex near-surface atmosphere [50].

It should be noted that no clearly quantitative relationship exists between the TVDI and SM because the true TVDI values are immeasurable. Although the TVDI has been widely used to estimate SM, the relationship between the TVDI and SM was estimated using empirical functions at the satellite scale [21]. Therefore, no fixed relationship exists between the TVDI and SM. This relationship is also influenced by the spatial resolution [57], window size [60], vegetation type and topography [58]. Therefore, this relationship may be unsuitable for airborne data with a spatial resolution of 3 m. In addition, it could be an unreasonable assumption that the dry edge represents the minimum SM and the wet edge represents the maximum SM for the TVDI. The T_s is an indicator of surface energy flux rather than SM [40]. Thus, the dry edge more likely represents the limiting values of surface evaporation rather than a purely dry soil surface [48].

The uncertainties in the $\Delta T_s/Fr$ space method for remotely sensed SM estimations should be emphasized. First, the representative dryness index of the $\Delta T_s/Fr$ space requires a full range of vegetation cover and SM availability. However, these conditions are difficult to achieve in most situations, particularly in small study areas. Second, uncertainties still exist in the validation of SM depth. Although a depth of 4 cm for the SM was indicated as suitable for validating the dryness index estimates in Section 5.2, the depth was determined from only 10 AWS measurements. The accuracy of the depth could be improved by using a greater number of field SM measurements at different layers. The depth used for the SM derived from the $\Delta T_s/Fr$ space also varies from thin to deeper layers as the fractional vegetation cover increases. This trend could result in errors when measurements taken at the same depth are used for validation. Third, the $\Delta T_s/Fr$ space method is ineffective in fully vegetated areas. Specifically, one assumption involving the development of the T_s/VI space is that the canopy temperature is insensitive to variations in SM in the surface and deep layers [61]. However, airborne

CASI/TASI SM estimations could be improved under a range of vegetation covers with help of microwave data, which are affected by canopies in only a limited fashion.

7. Conclusions

This study attempted to improve the performance of Ts/VI space on retrieving SM based on airborne CASI/TASI data with high spatial resolution to provide a fundamental basis for advancing the precision of SM estimations from optical satellite platforms based on the Ts/VI space algorithm. SM observations are important for promoting eco-hydrological research, improving runoff simulations and developing predictions in cold and arid regions. The $\Delta T_s/Fr$ space (incorporated with T_a) in airborne data revealed that the NDVI saturation and disturbed pixels interfere with the appropriate construction of the airborne $\Delta T_s/Fr$ space, which influences the accuracy of airborne SM estimations. As a result, the dry and wet edges were poorly extracted from the raw airborne $\Delta T_s/Fr$ space, as shown in Table 3. No significant relationships were found between the SM and raw dryness indices (TVDI and EF), with $r^2 < 0.24$. However, after adaptation of the $\Delta T_s/Fr$ space by adjusting the NDVI saturation and eliminating disturbed pixels, we observed that the accuracies of the extracted dry and wet edges were improved and the SM content was strongly correlated with the dryness indices from the non-disturbed $\Delta T_s/Fr$ space ($r^2 > 0.53$). Therefore, the adapted airborne $\Delta T_s/Fr$ space exhibited an improved performance for estimating SM.

The EF and TVDI estimates from the non-disturbed $\Delta T_s/Fr$ space were validated using the measured SM at a depth of 4 cm, which was determined by mixed land surfaces composed of bare soil and vegetated areas. The validation results showed that the EF approach outperformed the TVDI because it was better correlated with the measured SM (RMSE = $0.023 \text{ m}^3 \cdot \text{m}^{-3}$ and $r^2 = 0.67$).

This work indicates that airborne data with less sub-pixel heterogeneity can be used to assess the Ts/VI space algorithm developed from satellite observations. In addition, this assessment reveals that NDVI saturation in dense vegetation canopies and disturbed pixels should be evaluated and adapted when the Ts/VI algorithm is applied for estimating the SM from remote sensing data. By using LUCC data with similar or higher spatial resolutions and more detailed land use classification information, the coarse spatial resolution's disturbed pixels and the mixed pixels containing the disturbed land cover types can be discriminated and removed. This method may improve SM estimations based on optical satellite platforms and using the Ts/VI space algorithm.

The airborne results show that the EF could be used as an index for monitoring SM and dryness conditions due to its high sensitivity to SM. However, additional work is required to improve the accuracy of SM estimations under various vegetation covers, especially areas with high vegetative cover in which microwave data should be used. Moreover, the fine spatial details of airborne SM estimation enhance the scale consistency between the *in situ* measurements and the remotely sensed SM, which provide a promising method for validating coarse-scale microwave SM products and developing a SM downscaling algorithm.

Acknowledgments

This work was supported in part by the Natural Science Foundation of China under Grant 91125003 and in part by the National Basic Research Program of China under Grant 2013CB733401. The authors

would like to thank all of the scientists, engineers, and students who participated in the HiWATER campaigns, which provided airborne products and WSN data products for this work.

Author Contributions

Lei Fan was responsible for the data analysis and writing the manuscript. Qing Xiao contributed to the main research ideas, data collection and manuscript organization. Jianguang Wen and Qiang Liu contributed to the research ideas and data collection. Yong Tang, Dongqing You, Heshun Wang and Zhaoning Gong collected the field data and preprocessed the remote sensing data, and Xiaowen Li helped design the research. All of the authors thoroughly reviewed and edited this paper.

Conflicts of Interest

The authors declare no conflict of interest.

References

1. Gao, S.; Zhu, Z.; Liu, S.; Jin, R.; Yang, G.; Tan, L. Estimating the spatial distribution of soil moisture based on Bayesian maximum entropy method with auxiliary data from remote sensing. *Int. J. Appl. Earth Obs. Geoinf.* **2014**, *32*, 54–66.
2. Chen, F.; Avissar, R. Impact of land-surface moisture variability on local shallow convective cumulus and precipitation in large-scale models. *J. Appl. Meteorol.* **1994**, *33*, 1382–1401.
3. Kerr, Y.H.; Waldteufel, P.; Wigneron, J.-P.; Delwart, S.; Cabot, F.; Boutin, J.; Escorihuela, M.-J.; Font, J.; Reul, N.; Gruhier, C. The SMOS mission: New tool for monitoring key elements of the global water cycle. *Proc. IEEE* **2010**, *98*, 666–687.
4. Du, Y.; Ulaby, F.T.; Dobson, M.C. Sensitivity to soil moisture by active and passive microwave sensors. *IEEE Trans. Geosci. Remote Sens.* **2000**, *38*, 105–114.
5. Chauhan, N.; Miller, S.; Ardanuy, P. Spaceborne soil moisture estimation at high resolution: A microwave-optical/IR synergistic approach. *Int. J. Remote Sens.* **2003**, *24*, 4599–4622.
6. Dubois, P.C.; Van Zyl, J.; Engman, T. Measuring soil moisture with imaging radars. *IEEE Trans. Geosci. Remote Sens.* **1995**, *33*, 915–926.
7. Moran, M.; Clarke, T.; Inoue, Y.; Vidal, A. Estimating crop water deficit using the relation between surface-air temperature and spectral vegetation index. *Remote Sens. Environ.* **1994**, *49*, 246–263.
8. Carlson, T. An overview of the “Triangle Method” for estimating surface evapotranspiration and soil moisture from satellite imagery. *Sensors* **2007**, *7*, 1612–1629.
9. Saleh, K.; Kerr, Y.H.; Richaume, P.; Escorihuela, M.; Panciera, R.; Delwart, S.; Boulet, G.; Maisongrande, P.; Walker, J.; Wursteisen, P. Soil moisture retrievals at L-band using a two-step inversion approach (COSMOS/NAFE’05 Experiment). *Remote Sens. Environ.* **2009**, *113*, 1304–1312.
10. Sánchez, N.; Piles, M.; Martínez-Fernández, J.; Vall-llossera, M.; Pipia, L.; Camps, A.; Aguasca, A.; Pérez-Aragüés, F.; Herrero-Jiménez, C.M. Hyperspectral optical, thermal, and microwave L-band observations for soil moisture retrieval at very high spatial resolution. *Photogramm. Eng. Remote Sens.* **2014**, *80*, 745–755.

11. Panciera, R.; Walker, J.P.; Kalma, J.D.; Kim, E.J.; Hacker, J.M.; Merlin, O.; Berger, M.; Skou, N. The NAFE'05/CoSMOS data set: Toward SMOS soil moisture retrieval, downscaling, and assimilation. *IEEE Trans. Geosci. Remote Sens.* **2008**, *46*, 736–745.
12. Le Vine, D.M.; Lagerloef, G.S.; Torrusio, S.E. Aquarius and remote sensing of sea surface salinity from space. *Proc. IEEE* **2010**, *98*, 688–703.
13. Entekhabi, D.; Njoku, E.G.; O'Neill, P.E.; Kellogg, K.H.; Crow, W.T.; Edelstein, W.N.; Entin, J.K.; Goodman, S.D.; Jackson, T.J.; Johnson, J. The Soil Moisture Active Passive (SMAP) mission. *Proc. IEEE* **2010**, *98*, 704–716.
14. Li, Z.; Wang, Y.; Zhou, Q.; Wu, J.; Peng, J.; Chang, H. Spatiotemporal variability of land surface moisture based on vegetation and temperature characteristics in Northern Shaanxi Loess Plateau, China. *J. Arid Environ.* **2008**, *72*, 974–985.
15. Mallick, K.; Bhattacharya, B.K.; Patel, N. Estimating volumetric surface moisture content for cropped soils using a soil wetness index based on surface temperature and NDVI. *Agric. For. Meteorol.* **2009**, *149*, 1327–1342.
16. Merlin, O.; Chehbouni, A.G.; Kerr, Y.H.; Njoku, E.G.; Entekhabi, D. A combined modeling and multispectral/multiresolution remote sensing approach for disaggregation of surface soil moisture: Application to SMOS configuration. *IEEE Trans. Geosci. Remote Sens.* **2005**, *43*, 2036–2050.
17. Merlin, O.; Walker, J.P.; Chehbouni, A.; Kerr, Y. Towards deterministic downscaling of SMOS soil moisture using MODIS derived soil evaporative efficiency. *Remote Sens. Environ.* **2008**, *112*, 3935–3946.
18. Merlin, O.; Walker, J.P.; Kalma, J.D.; Kim, E.J.; Hacker, J.; Panciera, R.; Young, R.; Summerell, G.; Hornbuckle, J.; Hafeez, M. The NAFE'06 data set: Towards soil moisture retrieval at intermediate resolution. *Adv. Water Resour.* **2008**, *31*, 1444–1455.
19. Sobrino, J.; Franch, B.; Mattar, C.; Jimenez-Munoz, J.; Corbari, C. A method to estimate soil moisture from Airborne Hyperspectral Scanner (AHS) and ASTER data: Application to SEN2FLEX and SEN3EXP campaigns. *Remote Sens. Environ.* **2012**, *117*, 415–428.
20. Scheidt, S.; Ramsey, M.; Lancaster, N. Determining soil moisture and sediment availability at White Sands Dune Field, New Mexico, from apparent thermal inertia data. *J. Geophys. Res.: Earth Surf.* **2010**, *115*, doi: 10.1029/2009JF001378.
21. Sandholt, I.; Rasmussen, K.; Andersen, J. A simple interpretation of the surface temperature/vegetation index space for assessment of surface moisture status. *Remote Sens. Environ.* **2002**, *79*, 213–224.
22. Patel, N.; Anapashsha, R.; Kumar, S.; Saha, S.; Dadhwal, V. Assessing potential of MODIS derived temperature/vegetation condition index (TVDI) to infer soil moisture status. *Int. J. Remote Sens.* **2009**, *30*, 23–39.
23. Rahimzadeh-Bajgirani, P.; Omasa, K.; Shimizu, Y. Comparative evaluation of the Vegetation Dryness Index (VDI), the Temperature Vegetation Dryness Index (TVDI) and the improved TVDI (iTVDI) for water stress detection in semi-arid regions of Iran. *ISPRS J. Photogramm. Remote Sens.* **2012**, *68*, 1–12.
24. Wang, C.; Qi, S.; Niu, Z.; Wang, J. Evaluating soil moisture status in China using the temperature-vegetation dryness index (TVDI). *Can. J. Remote Sens.* **2004**, *30*, 671–679.

25. Gao, Z.; Gao, W.; Chang, N.-B. Integrating temperature vegetation dryness index (TVDI) and regional water stress index (RWSI) for drought assessment with the aid of LANDSAT TM/ETM+ images. *Int. J. Appl. Earth Obs. Geoinf.* **2011**, *13*, 495–503.
26. Petropoulos, G.; Carlson, T.; Wooster, M.; Islam, S. A review of Ts/VI remote sensing based methods for the retrieval of land surface energy fluxes and soil surface moisture. *Prog. Phys. Geogr.* **2009**, *33*, 224–250.
27. Thenkabail, P.S.; Smith, R.B.; De Pauw, E. Hyperspectral vegetation indices and their relationships with agricultural crop characteristics. *Remote Sens. Environ.* **2000**, *71*, 158–182.
28. Mutanga, O.; Skidmore, A.K. Narrow band vegetation indices overcome the saturation problem in biomass estimation. *Int. J. Remote Sens.* **2004**, *25*, 3999–4014.
29. Santin-Janin, H.; Garel, M.; Chapuis, J.-L.; Pontier, D. Assessing the performance of NDVI as a proxy for plant biomass using non-linear models: A case study on the Kerguelen archipelago. *Polar Biol.* **2009**, *32*, 861–871.
30. Gu, Y.; Wylie, B.K.; Howard, D.M.; Phuyal, K.P.; Ji, L. NDVI saturation adjustment: A new approach for improving cropland performance estimates in the Greater Platte River Basin, USA. *Ecol. Indic.* **2013**, *30*, 1–6.
31. Carlson, T.N.; Ripley, D.A. On the relation between NDVI, fractional vegetation cover, and leaf area index. *Remote Sens. Environ.* **1997**, *62*, 241–252.
32. Li, X.; Cheng, G.; Liu, S.; Xiao, Q.; Ma, M.; Jin, R.; Che, T.; Liu, Q.; Wang, W.; Qi, Y. Heihe Watershed Allied Telemetry Experimental Research (HiWATER): Scientific objectives and experimental design. *Bull. Am. Meteorol. Soc.* **2013**, *94*, 1145–1160.
33. Kim, G.; Barros, A.P. Downscaling of remotely sensed soil moisture with a modified fractal interpolation method using contraction mapping and ancillary data. *Remote Sens. Environ.* **2002**, *83*, 400–413.
34. Jin, R.; Li, X.; Yan, B.; Luo, W.; Ma, M.; Guo, J.; Kang, J.; Zhu, Z.; Zhao, S. A nested ecohydrological wireless sensor network for capturing the surface heterogeneity in the midstream areas of the Heihe River Basin, China. *IEEE Geosci. Remote Sens. Lett.* **2014**, *11*, 2015–2019.
35. Kang, J.; Li, X.; Jin, R.; Ge, Y.; Wang, J.; Wang, J. Hybrid optimal design of the eco-hydrological wireless sensor network in the middle reach of the Heihe River Basin, China. *Sensors* **2014**, *14*, 19095–19114.
36. Xiao, Q.; Wen, J. HiWATER: Visible and Near-Infrared Hyperspectral Radiometer (7th, July, 2012). Available online: <http://dragon2lrc10.westgis.ac.cn/data/f0b641b4-d7a8-4186-a002-7f7078d96103> (accessed on 7 July 2012)
37. Xiao, Q.; Wen, J. HiWATER: Thermal-Infrared Hyperspectral Radiometer (10th, July, 2012). Available online: <http://card.westgis.ac.cn/data/b26addec-dde4-4a6f-80ef-505041c45a7a> (accessed on 10 July 2012).
38. Berk, A. Voigt equivalent widths and spectral-bin single-line transmittances: Exact expansions and the MODTRAN[®]5 implementation. *J. Quant. Spectrosc. Radiat. Transf.* **2013**, *118*, 102–120.
39. Wang, H.; Xiao, Q.; Li, H.; Zhong, B. Temperature and emissivity separation algorithm for TASI airborne thermal hyperspectral data. In Proceedings of 2011 International Conference on Electronics, Communications and Control (ICECC), Ningbo, China, 9–11 September 2011; pp. 1075–1078.

40. Wang, K.; Li, Z.; Cribb, M. Estimation of evaporative fraction from a combination of day and night land surface temperatures and NDVI: A new method to determine the Priestley-Taylor parameter. *Remote Sens. Environ.* **2006**, *102*, 293–305.
41. Sun, Z.; Wang, Q.; Matsushita, B.; Fukushima, T.; Ouyang, Z.; Watanabe, M. A new method to define the VI-Ts diagram using subpixel vegetation and soil information: A case study over a semiarid agricultural region in the north China plain. *Sensors* **2008**, *8*, 6260–6279.
42. Nishida, K.; Nemani, R.R.; Running, S.W.; Glassy, J.M. An operational remote sensing algorithm of land surface evaporation. *J. Geophys. Res.: Atmos.* **2003**, *108*, doi:10.1029/2002JD002062.
43. Jackson, R.D.; Idso, S.; Reginato, R.; Pinter, P. Canopy temperature as a crop water stress indicator. *Water Resour. Res.* **1981**, *17*, 1133–1138.
44. Chen, C.-F.; Son, N.-T.; Chang, L.-Y.; Chen, C.-C. Monitoring of soil moisture variability in relation to rice cropping systems in the Vietnamese Mekong Delta using MODIS data. *Appl. Geogr.* **2011**, *31*, 463–475.
45. Rahimzadeh-Bajgiran, P.; Berg, A.A.; Champagne, C.; Omasa, K. Estimation of soil moisture using optical/thermal infrared remote sensing in the Canadian Prairies. *ISPRS J. Photogramm. Remote Sens.* **2013**, *83*, 94–103.
46. Tucker, C.J. Red and photographic infrared linear combinations for monitoring vegetation. *Remote Sens. Environ.* **1979**, *8*, 127–150.
47. Gutman, G.; Ignatov, A. The derivation of the green vegetation fraction from NOAA/AVHRR data for use in numerical weather prediction models. *Int. J. Remote Sens.* **1998**, *19*, 1533–1543.
48. Jiang, L.; Islam, S. Estimation of surface evaporation map over southern Great Plains using remote sensing data. *Water Resour. Res.* **2001**, *37*, 329–340.
49. World Meteorological Organization (WMO). *Guide to Meteorological Instruments and Methods of Observation*; WMO-No. 8; WMO: Geneva, Switzerland, 2008.
50. Lee, T.J.; Pielke, R.A. Estimating the soil surface specific humidity. *J. Appl. Meteorol.* **1992**, *31*, 480–484.
51. Merlin, O.; Al Bitar, A.; Walker, J.P.; Kerr, Y. An improved algorithm for disaggregating microwave-derived soil moisture based on red, near-infrared and thermal-infrared data. *Remote Sens. Environ.* **2010**, *114*, 2305–2316.
52. Wagner, W.; Lemoine, G.; Rott, H. A method for estimating soil moisture from ERS scatterometer and soil data. *Remote Sens. Environ.* **1999**, *70*, 191–207.
53. Verstraeten, W.W.; Veroustraete, F.; van der Sande, C.J.; Grootaers, I.; Feyen, J. Soil moisture retrieval using thermal inertia, determined with visible and thermal spaceborne data, validated for European forests. *Remote Sens. Environ.* **2006**, *101*, 299–314.
54. Zhihui, W.; Liangyun, L. Monitoring on land cover pattern and crops structure of oasis irrigation area of middle reaches in Heihe River Basin using remote sensing data. *Adv. Earth Sci.* **2013**, *28*, 948–956.
55. Xiao, Q.; Wen, J. HiWATER: Vegetation Height Product in the Middle Reaches of the Heihe River Basin (19 July 2012). Available online: <http://dragon2lrc10.westgis.ac.cn/data/6b4f1a86-9b2b-42c3-90e2-6c51358bce69> (accessed on 19 July 2012).

56. Weng, Q.; Lu, D. A sub-pixel analysis of urbanization effect on land surface temperature and its interplay with impervious surface and vegetation coverage in Indianapolis, United States. *Int. J. Appl. Earth Obs. Geoinf.* **2008**, *10*, 68–83.
57. Merlin, O.; Escorihuela, M.J.; Mayoral, M.A.; Hagolle, O.; Al Bitar, A.; Kerr, Y. Self-calibrated evaporation-based disaggregation of SMOS soil moisture: An evaluation study at 3 km and 100 m resolution in Catalunya, Spain. *Remote Sens. Environ.* **2013**, *130*, 25–38.
58. Sun, Z.; Wang, Q.; Matsushita, B.; Fukushima, T.; Ouyang, Z.; Watanabe, M.; Gebremichael, M. Evaluation of the VI-Ts method for estimating the land surface moisture index and air temperature using ASTER and MODIS data in the North China Plain. *Int. J. Remote Sens.* **2011**, *32*, 7257–7278.
59. Sharp, R.; Davies, W. Root growth and water uptake by maize plants in drying soil. *J. Exp. Bot.* **1985**, *36*, 1441–1456.
60. Nemani, R.; Pierce, L.; Running, S.; Goward, S. Developing satellite-derived estimates of surface moisture status. *J. Appl. Meteorol.* **1993**, *32*, 548–557.
61. Tang, R.; Li, Z.-L.; Tang, B. An application of the Ts-VI triangle method with enhanced edges determination for evapotranspiration estimation from MODIS data in arid and semi-arid regions: Implementation and validation. *Remote Sens. Environ.* **2010**, *114*, 540–551.

© 2015 by the authors; licensee MDPI, Basel, Switzerland. This article is an open access article distributed under the terms and conditions of the Creative Commons Attribution license (<http://creativecommons.org/licenses/by/4.0/>).